南京航空航天大学

论　文　集

（一九九九年）

第6册

（二系）

南京航空航天大学科技部编

二〇〇〇年三月

二　　系

目　录

二〇四教研室(19 篇)

二〇五教研室(18篇)

Inviscid and viscous simulations of spoiler performance

C. Xu
Department of Mechanical Engineering
University of Wisconsin, Milwaukee, USA

W. W. H. Yeung
School of Mechanical and Production Engineering
Nanyang Technological University, Singapore

R. W. Guo
Department of Power Engineering
Nanjing University of Aeronautics and Astronautics, China

ABSTRACT

Inviscid and viscous computational models have been used to predict two-dimensional steady separated flow around an aerofoil with a spoiler. First, an attempt is made to construct an inviscid panel method in which piece-wise linear vortex panels are placed on the aerofoil and spoiler. The separated region is modelled with potential flow analysis by using free vortex sheets placed on the separation streamline from the spoiler tip and aerofoil trailing-edge. The shapes of the vortex sheets require an iteration to be established. The calculation is based on an assumption of the length of the free vortex sheets. Second, a viscous procedure based on a finite control volume scheme is used to solve the Navier-Stokes equations for turbulent flow by making used of the k-ε model. An algebraic pressure correction is incorporated in the calculation. The predictions from the two models are in reasonable agreement with experimental measurements.

NOMENCLATURE

c	aerofoil chord
C_p	pressure coefficient
b	aerofoil thickness
e	spoiler chordwise location
[illegible]	wake length factor
h	spoiler height
H_w	height of wake
J	total flux
$\mathbf{J}$	Jacobian matrix
k	turbulence kinetic energy
L_w	length of wake
p	static pressure
Re	Reynolds number
$R_n(\phi)$	residual of variable ϕ
S	source term
V	velocity $= (u,v)$
V_∞	freestream velocity
α	aerofoil incidence or relaxation parameter
ρ	fluid density
μ	effective viscosity
γ	strength of bound vortex or vortex sheet
ε	energy dissipation
ϕ	general variable
Γ_ϕ	exchange coefficient

1.0 INTRODUCTION

A spoiler, as the name implies, is a control surface located on the upper surface of a wing which 'spoils' the flow, such that the overall load is modified when it is deflected. A spoiler can act as a pure air brake, a symmetric direct lift control or an asymmetric roll control.

The flow associated with the wing–spoiler configuration is very complex and includes separation, reattachment and vortex shedding[1, 2]. The interaction between the vortices from the spoiler tip and the trailing-edge results in a turbulent oscillatory wake which affects the effectiveness of the spoiler and other control surfaces. It has been recognised that large vortical structures are the dominant features in these flows and the unsteady effects produced can be beneficial or detrimental to the overall performance of the wing.

There has been substantial theoretical work on spoiler flows, especially with the inviscid assumption. The earliest theoretical modelling of the inviscid steady flow around an aerofoil–spoiler–flap system was by Woods[3], who used a free streamline theory based on the method of linear perturbations to predict aerodynamic load. The theory assumes that the wake behind the spoiler has a uniform pressure and that it extends behind the aerofoil trailing-edge. The magnitude of this pressure is taken from experimental measurements. As usual with theories of linear perturbations, it is restricted to thin aerofoils at low incidence with small spoiler height and inclination. Barnes[4] extended Woods' theory to predict the aerodynamic characteristics of a normal spoiler, modifying the effective spoiler height to account

Paper No. 2278. Manuscript received 17 April 1997, revised version received 29 July 1997, accepted 16 April 1998.

for the boundary layer displacement thickness at the spoiler location. Again, an empirical spoiler base pressure was assumed.

Jandali and Parkinson[5] developed another potential flow model based on conformal mapping and the use of mathematical singularities for thick aerofoils with spoilers normal to the aerofoil surface. Recently, Parkinson and Yeung[6] proposed a new mapping sequence and extended the model to include spoilers of arbitrary inclination. Similar to the theory developed by Woods, the models by Jandali and Parkinson, Parkinson and Yeung require the spoiler base-pressure as an input in the calculation. Therefore, knowledge of the base-pressure either from theoretical predictions or experimental measurements is necessary. Because of the need to use particular empirical data, their methods are rather awkward to apply.

Tou and Hancock[7] formulated a panel method with two free vortex sheets simulating the shear layers from the spoiler tip and the trailing-edge to study the steady spoiler characteristics. To close these vortex sheets, two discrete vortices of equal strength but opposite in sign are introduced at the ends of the sheets. The extent of the continuous vortex sheet after the aerofoil trailing-edge is the empirical parameter, instead of the base-pressure as found in other models. The lengths of these vortex sheets are assumed not to change with the aerofoil incidence, spoiler height and inclination.

A method for calculating the flow about aerofoils up to and beyond the stall was developed by Maskew and Dvorak[8]. The separated region was modelled in the potential flow analysis by using free vortex sheets. An assumption of estimating the length of a free vortex sheet was made. A tentative correlation curve for wake fineness ratio, i.e. aerofoil thickness/chord, was proposed. However, the method has not been further developed to deal with the problem of flow over an aerofoil with a spoiler. An aim of the current investigation is to incorporate the above-mentioned model into an inviscid panel method to predict the steady two-dimensional spoiler flow. The standard first-order vortex panel method[9] has been applied in the present calculation together with a wake length model.

Computational fluid dynamics (CFD) has become a popular tool for simulating complicated flow problems. However, many aspects related to CFD, such as the pressure-correction scheme, turbulence model, mesh-generation and discretisation scheme, still require further refinements. The finite-difference equations obtained from the governing equations form a coupled nonlinear system. With the pressure correction procedure, the iterative scheme adopted is such that the momentum equations become uncoupled and can be solved sequentially in terms of an applied pressure field. Various pressure correction schemes have been proposed and developed. Most of pressure correction schemes need to solve the difference equation of the correction pressure. However, because of the complicated form of the pressure correction equation and the nonlinear nature of the problem, a procedure based on a difference form of the correction pressure equation could be inefficient. In this study, Navier-Stokes computations based on the k-ε turbulence model are used together with an algebraic pressure correction method for the velocity–pressure coupling. Results from the inviscid and viscous computations are compared with experimental data[5,6,10].

2.0 INVISCID CALCULATION

2.1 Outline of the panel method

The panel method is an established part of computational aerodynamics. Basic foundations for attached flow have been soundly laid, complemented by extensive knowledge derived from *ad hoc* experience. The application of numerical techniques allows the adequate treatment of complex geometrical bodies and the fulfillment of boundary conditions at the surface. The solution of the flowfield can be reduced to determine the strengths of singularity elements distributed on the body's surface. This approach is more economical, from the computational point of view, than methods that solve for the flowfield in the whole fluid domain.

The first step in the panel method is to define the elements which replace the aerofoil surface. One obvious method is to let the coordinates of the surface be the end points of the elements. However, this has the disadvantage that the number of coordinates may be insufficient and that the coordinates may be irregularly spaced. Here, as suggested by Lewis[9], the x-coordinates of the end points of the surface elements are given by

$$x_n = c(1 - Cos(\varphi_n))/2 \qquad (n = 0, 1, \ldots, M) \qquad \ldots (1)$$

where $\varphi = 2\pi n/M$, c the aerofoil chord, and M an even number in order that an end point be located at the trailing-edge of an aerofoil. With this distribution, the x-coordinates of the elements on the upper surface are the same as those on the lower surface.

The aerofoil/spoiler surface is modelled by a finite number of straight line elements, or panels. Also, a distribution of vortices having a linear strength is placed over each element. By satisfying the boundary condition at each collocation point, a set of linear equations can be expressed as

$$\sum_{q=1}^{N} K_{pq}\gamma_q = -V_\infty(\mathrm{Cos}\alpha\mathrm{Sin}\beta_p - \mathrm{Sin}\alpha\mathrm{Cos}\beta_p) \qquad \ldots (2)$$

where K_{pq} are the coupling coefficients for elements p and q, N is the number of nodal points, α is the angle-of-attack, and β_p is the inclination of panel p. Detail of the panel method, including the Kutta condition, can be found in Lewis[9].

2.2 Representation of free shear layers

2.2.1 Basic assumptions

Separation can be classified into one of two types: bubble and free shear layer. Two-dimensional separated flows involving free shear layers have been investigated by Lewis[9] by using the discrete vortex method. The bubble type of separation involving reattachment, is seen in two-dimensional flow around aerofoils, aerofoil–spoiler flow, three-dimensional flow in the trailing-edge region of wings and rotors at incidence, and flow around bluff bodies having finite wake lengths. Recently, the bubble type of separation has received considerable attention[4-9]. Most of the methods employ sources to simulate the separated flow with the assumption that the pressure in the separated region is constant everywhere[4-8]. To implement this study, the vortex-panel method has been used to model this kind of separated flow. The basic assumptions of the method are:

1. boundary layers and free shear layers have no significant thickness,
2. the wake does not have any significant vorticity but has a constant total pressure, and
3. there is a total pressure loss across the vortex sheet.

The zero static pressure drop across each free shear layer can be used to obtain an expression for the total pressure in the wake in terms of the strength of the free vortex sheet. Consider the separation streamline from the trailing-edge. If the velocities inside and outside the vortex sheet are V_i and V_o respectively, then the average velocity in the layer is denoted by

$$V_a = 0 \cdot 5(V_i - V_o) \qquad \ldots (3)$$

Accordingly, the strength of this vortex sheet is

$$\gamma = V_i - V_o \qquad \ldots (4)$$

Applying the Bernoulli's equation, the jump in total pressure Δh across the shear layer can be written as

$$\Delta h = \rho\gamma V_a \qquad \ldots (5)$$

where ρ is the fluid density. The pressure coefficient is calculated from the velocities according to the Bernoulli's equation

$$C_p = 1 - \frac{V^2}{V_\infty^2} - 2\frac{\Delta h}{\rho V_\infty^2} \qquad \ldots (6)$$

where V is the local total velocity and V_∞ is the freestream. Note that $\Delta h = 0$ everywhere except in the wake region.

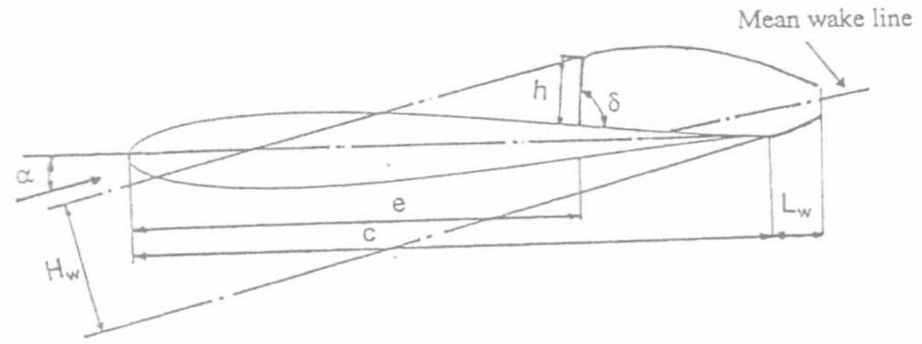

Figure 1. Inviscid flow model.

2.2.2 Wake simulation

The basic model used in this investigation is shown in Fig. 1. The flowfield can be constructed by adding to the uniform stream the so-called induced velocity associated with a vorticity distribution of strength equal to the curl of the velocity field. For simulating the separated flow, there are continuous thin vortex sheets emanating from the spoiler tip and aerofoil trailing-edge. To close the separation bubble, Tou and Hancock[7] introduced two discrete vortices of equal strength but opposite in sign. It is necessary to introduce the conceptual cuts in the flow to connect the vortex sheets to the discrete vortices and the discrete vortices to each other. Finally, the empirical length L_W of the trailing-edge vortex sheet is introduced and assumed to be $0{\cdot}2c$. The locations and strengths of the discrete vortices are chosen somewhat arbitrarily. In the present model, the method of using two vortices to close the wake is not used. Instead, the wake is assumed to have a finite length L_W, which is a linear function of the wake height H_W, that is

$$L_w = fH_w \qquad \ldots (7)$$

where f is the wake length factor. The linear relationship[8] between f and c/b is shown in Fig. 2. In this way, the wake length varies with the length of the spoiler and the angle-of-attack of the aerofoil. Shapes of the two vortex sheets can be determined through an iterative process. Initially, the streamlines are not known and the shapes of the wake must be obtained from an initial assumption. Here, the upper and lower sheets are represented by parabolic curves passing from the separation point to a common point downstream and the common point downstream is located on the mean wake line.

2.3 Solution procedure

The steps of the iterative process are described below.

1. The shapes of the free vortex sheets are guessed. Then, the strengths of the bound vortices and vortex sheets are calculated.
2. From the calculation of vortices, the velocity components outside each sheet are calculated and the new shapes of the sheets are computed so that they follow the flow direction.
3. The shape of each sheet and the strengths of the bound vortices and each sheet are updated.
4. The procedure will terminate if the shapes of the sheets do not differ much from the last calculation. Otherwise, steps 2. and 3. will be repeated.

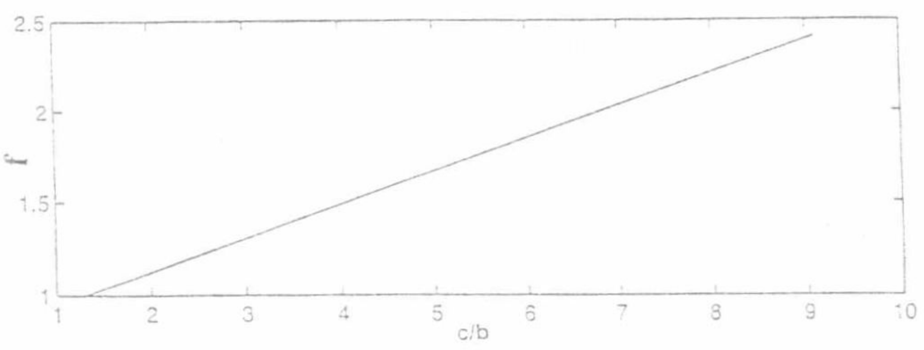

Figure 2. Variation of wake length factor with chord thickness[8].

3.0 NAVIER-STOKES SOLUTION

3.1 Governing equations

In cartesian tensor notation with the repeated-suffix summation convention, the equations governing the dynamics and mass transfer of a steady, turbulent fluid can be written as follows: mass conservation

$$\frac{\partial}{\partial x_j}(\rho u_j) = 0 \qquad \ldots (8)$$

Momentum conservation

$$\frac{\partial \rho u_i u_j}{\partial x_j} = -\frac{\partial p}{\partial x_i} + \frac{\partial \tau_{ij}}{\partial x_j} + f_i \qquad \ldots (9)$$

Here u_i is the velocity and f_i is the body force, both of the x_i component, and p is the pressure. In this study, no body force acts on the aerofoil and spoiler so f_i is zero. The deformation stress τ_{ij} is given by

$$\tau_{ij} = \mu\left(\frac{\partial u_i}{\partial x_j} + \frac{\partial u_j}{\partial x_i} + \frac{\partial u_l}{\partial x_l}\right) + \frac{2}{3}\mu\delta_{ij}\frac{\partial u_l}{\partial x_l} \qquad \ldots (10)$$

where δ_{ij} is the Kronecker delta. The effective viscosity is

$$\mu = \mu_l + \mu_t \qquad \ldots (11)$$

where μ_l and μ_t are respectively the laminar viscosity and turbulent viscosity.

In the dimensional form, the Navier-Stokes equations can be written as

$$\frac{\partial F}{\partial x} + \frac{\partial G}{\partial y} = \frac{\partial F_v}{\partial x} + \frac{\partial G_v}{\partial y} \qquad \ldots (12)$$

where

$$F = \begin{bmatrix} \rho u \\ \rho u^2 + p \\ \rho uv \end{bmatrix} \qquad G = \begin{bmatrix} \rho v \\ \rho uv \\ \rho v^2 + p \end{bmatrix}$$

$$F_v = \frac{1}{\mathrm{Re}}\begin{bmatrix} 0 \\ 2\mu\frac{\partial u}{\partial x} - \frac{2}{3}\mu\left(\frac{\partial u}{\partial x} + \frac{\partial v}{\partial y}\right) \\ \mu\left(\frac{\partial u}{\partial x} + \frac{\partial v}{\partial y}\right) \end{bmatrix} \qquad G_v = \frac{1}{\mathrm{Re}}\begin{bmatrix} 0 \\ \mu\left(\frac{\partial u}{\partial x} + \frac{\partial v}{\partial y}\right) \\ 2\mu\frac{\partial v}{\partial y} - \frac{2}{3}\mu\left(\frac{\partial u}{\partial x} + \frac{\partial v}{\partial y}\right) \end{bmatrix}$$

The set of equations in (12) constitutes the mathematical representation of the Reynolds average values of the flow properties. For solving the above mentioned equations, additional equations for modelling turbulence are given in the next section.

3.2 Turbulence model

3.2.1 k-ε model

Turbulence equations can be derived from the Navier-Stokes equations[11]. For example, turbulence kinetic energy equation in two dimensions

$$\frac{\partial}{\partial x}(\rho uk) + \frac{\partial}{\partial y}(\rho vk) = \frac{\partial}{\partial x}\left(\frac{\mu}{\sigma_k}\frac{\partial k}{\partial x}\right) + \frac{\partial}{\partial y}\left(\frac{\mu}{\sigma_k}\frac{\partial k}{\partial y}\right) + (G_k - \rho\varepsilon) \qquad \ldots (13)$$

energy dissipation equation

$$\frac{\partial}{\partial x}(\rho u\varepsilon) + \frac{\partial}{\partial y}(\rho u\varepsilon) = \frac{\partial}{\partial x}\left(\frac{\mu}{\sigma_\varepsilon}\frac{\partial \varepsilon}{\partial x}\right) + \frac{\partial}{\partial y}\left(\frac{\mu}{\sigma_\varepsilon}\frac{\partial \varepsilon}{\partial y}\right) + \frac{\varepsilon}{k}(c_1 G_k - c_2\rho\varepsilon) \qquad \ldots (14)$$

where G_k is the generation term given by

$$G_k = \mu_t \left\{ 2\left[\left(\frac{\partial u}{\partial x}\right)^2 + \left(\frac{\partial v}{\partial y}\right)^2\right] + \left(\frac{\partial u}{\partial y} + \frac{\partial v}{\partial x}\right)^2 \right\} \quad \ldots (15)$$

The turbulent viscosity is related to k and ε via

$$\mu_t = c_d \rho \frac{k^2}{\varepsilon} \quad \ldots (16)$$

The empirical parameters of the k-ε model are

$\sigma_k = 1 \cdot 0$, $\sigma_\varepsilon = 1 \cdot 22$, $c_1 = 1 \cdot 44$, $c_2 = 1 \cdot 92$, $c_d = 0 \cdot 09$

3.2.2 Wall function

In general, the k-ε model is suitable in regions where the flow is entirely turbulent. However, viscous effects become dominant near a solid surface. Experience shows that the k-ε model does not lead to acceptable predictions near a solid surface. For numerical computations, there are two main methods for treating the adjacent wall regions more carefully; one is to use the wall function and the other is the low-Reynolds-number model. In the present calculation, the wall function or the law of the wall[11, 12] has been used.

The region close to a solid wall can be divided into two sub-layers: one is the laminar or viscous sub-layer where viscous effects are dominant and the other is the turbulent sub-layer. Suppose the first computational point P close to the wall is in the turbulent sub-layer. At this point, the velocity U_p is parallel to the solid boundary and has a logarithmic variation given by

$$|U_p| = \frac{u^*}{K} \ln\left(E y_p^+\right) \quad \ldots (17)$$

where u^* is the friction velocity, and y_p^+ represents a non-dimensional distance between P and the wall. They are defined by

$$u^* = \left(\frac{\tau_w}{\rho}\right)^{0 \cdot 5} \quad \ldots (18)$$

$$y_p^+ = \frac{\rho y_p u^*}{\mu_t} \quad \ldots (19)$$

where τ_w is the shear stress at the wall, K (= 0·4) is the von Karman constant, E (= 9·7) is a roughness parameter and y_p is the actual dimensional distance. y_p^+ sets the limits between different sub-layers. If the turbulent sub-layer is in local equilibrium, then the rate of ε-production is exactly equal to its rate of destruction. This leads to

$$\varepsilon = \frac{\mu_t}{\rho}\left(\frac{\partial u}{\partial y}\right)^2 \quad \ldots (20)$$

If the shear stress is further assumed to be constant in the sub-layer ($\tau_p = \tau_w$), then by using the logarithmic law, it is found that

$$k = \frac{u^{*2}}{\sqrt{c_d}} \quad \ldots (21)$$

$$\varepsilon = \frac{u^{*3}}{k y_p} \quad \ldots (22)$$

The above equations give the values of k and ε at point P without solving the transport equations. These values are used to calculate the turbulent viscosity and serve as boundary conditions for the rest of the domain. It is not necessary to calculate k and ε at the wall. The viscosity there is equal to laminar viscosity.

3.3 Finite difference equations

The general form of the differential equations governing a steady, two-dimensional flow can be written as

$$\frac{\partial}{\partial x}(\rho u \phi) + \frac{\partial}{\partial y}(\rho v \phi) = \frac{\partial}{\partial x}\left(\Gamma_\phi \frac{\partial \phi}{\partial x}\right) + \frac{\partial}{\partial y}\left(\Gamma_\phi \frac{\partial \phi}{\partial y}\right) + S_\phi \quad \ldots (23)$$

where ϕ is a general variable, and Γ_ϕ is the exchange coefficient for the property ϕ. S_ϕ is the source expression for ϕ, which, in the most general form, may comprise a term for the rate of generation of ϕ per unit volume together with other terms that cannot be included in the terms on the left-hand side of the equation.

In the calculation, the governing equations are transformed from the physical domain (x, y) to the computational domain (ξ, η). A general transformation is used in the following form[13]

$$\xi = \xi(x, y) \quad \ldots (24)$$

$$\eta = \eta(x, y) \quad \ldots (25)$$

The Jacobian matrix for transformation can be written as

$$J = \frac{\partial(\xi, \eta)}{\partial(x, y)} = \frac{1}{x_\xi y_\eta - x_\eta y_\xi} \quad \ldots (26)$$

and

$$\xi_x = J y_\eta \qquad \eta_x = -J y_\xi \quad \ldots (27)$$

$$\xi_y = -J x_\eta \qquad \eta_y = J x_\xi \quad \ldots (28)$$

Substituting Equations (27) and (28) into Equation (23) gives the following equation (with details given in Amano[13], Patankar *et al*[14] and Pun and Spalding[15])

$$\frac{\partial}{\partial \xi}(\rho \tilde{u} \tilde{\phi}) + \frac{\partial}{\partial \eta}(\rho \tilde{u} \tilde{\phi}) = \frac{\partial}{\partial \xi}\left(\tilde{\Gamma}_\phi \frac{\partial \tilde{\phi}}{\partial \xi}\right) + \frac{\partial}{\partial \eta}\left(\tilde{\Gamma}_\phi \frac{\partial \tilde{\phi}}{\partial \eta}\right) + \tilde{S}_\phi \quad \ldots (29)$$

where

$$\tilde{u} = u\xi_x + v\xi_y \qquad \tilde{v} = u\eta_x - v\eta_y \quad \ldots (30)$$

Note that (~) in Equation (29) is usually dropped for simplicity and it has a form similar to Equation (23).

The staggered grid method[14] has been used in the calculation. While the scalar quantities are stored at the intersections of the grid lines, the velocity components are stored midway between adjacent grid nodes, as shown in Fig. 3. A finite difference equation linking the value of ϕ at point P to those at the four neighboring nodes (N, E, W and S) is obtained by integrating Equation (29) over the volume of the cell. From this the diffusion and convection terms are obtained. The total flux through the west face of the cell is $J_{\phi,w}$ and

$$a_w J_{\phi,w} = (D_w + C_w)\phi_w - D_w \phi_p \qquad \text{if } C_w \geq 0$$
$$a_w J_{\phi,w} = D_w \phi_w - (D_w - C_w)\phi_p \qquad \text{otherwise} \quad \ldots (31)$$

In these expressions, a_w is the area of the west cell-face and

$$D_w = \frac{\frac{1}{2} a_w \left(\Gamma_{\phi,w} + \Gamma_{\phi,P}\right)}{\xi_p - \xi_w} \quad \ldots (32)$$

$$C_w = (\rho u a)_w \quad \ldots (33)$$

Equation (32) can be written as

$$a_w J_{\phi,w} = A_w^\phi(\phi_w - \phi_p) + C_w \phi_p \quad \ldots (34)$$

where

$$A^\phi_w = \text{Max}(D_w, D_w + C_w) \quad \ldots (35)$$

Total flux expressions for the other three cell faces can be similarly obtained. By a suitable combination of these four expressions, the net

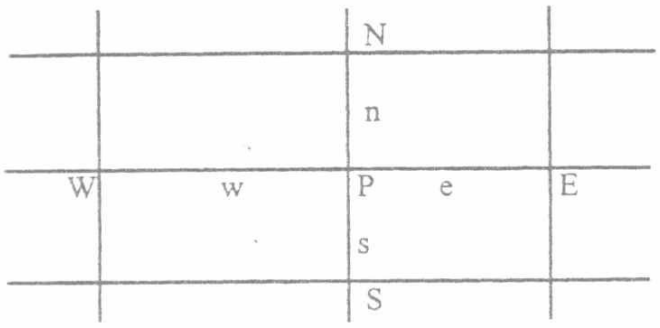

Figure 3. The staggered grid.

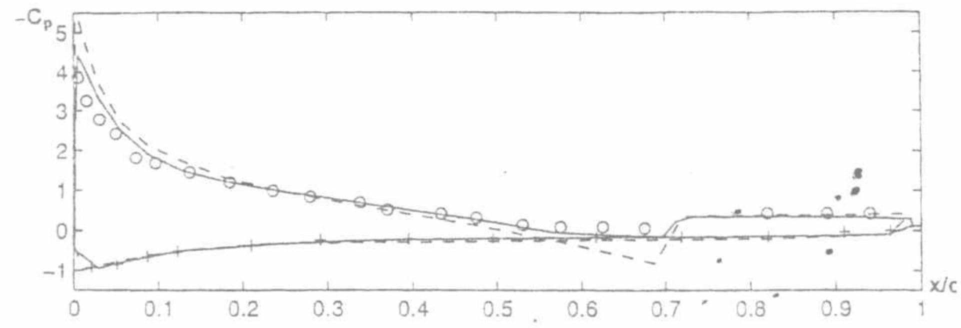

Figure 4. Pressure distributions on Joukowski aerofoil, $h = 0{\cdot}1c$, $e = 0{\cdot}7c$, $\delta = 90°$
(-- panel method; — N–S; +o experimental[5])

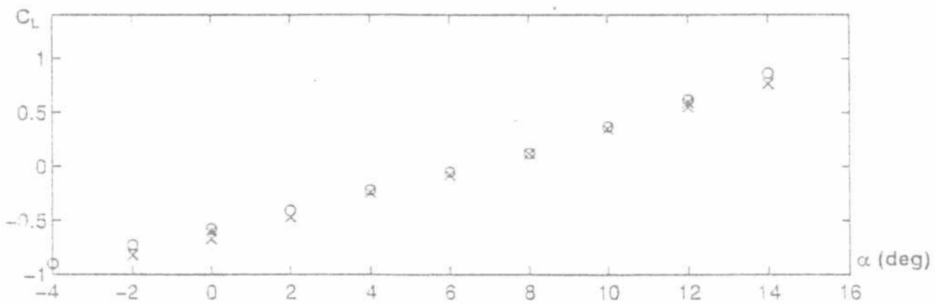

Figure 5. Lift versus angle-of-attack, $h = 0{\cdot}1c$, $e = 0{\cdot}7c$, $\delta = 90°$
(x panel method; * N–S; +o experimental)

outflow of ϕ by diffusion and convection can be obtained. Equating this to the volume integral of the source term, S^ϕ_p, and making use of the mass continuity leads to the finite difference form

$$\phi_p = \frac{\left[\sum_i \left(A_i^\phi \phi_i\right) + S_p^\phi\right]}{\sum_i A_i^\phi} \qquad \ldots (36)$$

where the sum is over the four neighbouring nodes, N, E, S and W. Patankar and Spalding[15] introduced under-relaxation into Equation (36) as follows

$$\phi_p = (1-\alpha)\phi_p^* + \alpha\left\{\frac{\left[\sum_i \left(A_i^\phi \phi_i\right) + S_p^\phi\right]}{\sum_i A_i^\phi}\right\} \qquad \ldots (37)$$

where ϕ_p^* is the value of ϕ_p from the previous cycle and α is a relaxation parameter. In the present calculation, $\alpha = 0{\cdot}2$ for pressure equation and $\alpha = 0{\cdot}7$ for other variables.

3.4 Pressure correction equations

In the present method, the conservation of mass is enforced, as in SIMPLE[15], via a pressure correction step at which the finite difference equations have to be set up. From the guessed values of the pressure field, a first approximation to the velocity field (u^*, v^*) can be found. However, u^* and v^* will not generally satisfy the continuity equation. The pressure and velocity fields are then corrected so that the continuity and momentum equations are satisfied. The pressure p and velocity field (u, v) are written in terms of their previous values p^*, u^* and v^*, and corrections p', u' and v' as follows

$$p = p^* + p' \qquad \ldots (38)$$

$$u = u^* + u' \qquad \ldots (39)$$

$$v = v^* + v' \qquad \ldots (40)$$

where u and v are required to satisfy the continuity equation. Substituting (39) and (40) into the continuity equation gives

$$\nabla \bullet (V') = -\nabla \bullet \left(V^*\right) \qquad \ldots (41)$$

The equation for the pressure correction, which can be obtained from Equations (38) to (41) and momentum equations (with the details given in Xu and Guo[16]) is

$$A_p p_p' = A_s p_s' + A_w p_w' - \Delta\xi\Delta\eta\nabla \bullet V^* \qquad \ldots (42)$$

where A_p, A_s and A_w are coefficients involving areas and coefficients linking pressure differences to corresponding velocities. It should be noted that p_s' and p_w' are upwind direction pressure corrections with reference to the flow direction. Therefore, the present method is an algebraic method.

3.5 Solution of finite difference equations

The finite difference equations for a particular variable along a grid line are solved by the tri-diagonal matrix algorithm (TDMA)[15,16] with values of the variable on both sides of the line kept unchanged. This operation is repeated for all variables on the line before the next line is visited. A typical sweep of the field for solving the algorithm equation involves the following steps

(i) provide initial guessed values of variables in the field.
(ii) find values of u^* and v^* using the existing pressure field, i.e. p^*,
(iii) compute values of p' and hence obtain final values of u, v and p.
(iv) solve for k and ε and update the turbulent viscosity,
(v) update values of all variables, and
(vi) repeat steps *(ii)* to *(v)* until the values in the whole field converge.

In this calculation, the maximum numbers of the local iterative sweeps are 500 and 100 for pressure and other variables. The numerical convergence is monitored through residuals. A residual of the variable ϕ at a node P, denoted by $R_p(\phi)$ is here defined by

$$R_p(\phi) = \phi_p \sum_i A_i^\phi - \sum_i A_i^\phi \phi_{ii} - S_p^\phi \qquad \ldots (43)$$

The residuals in local sweeps are equal to 0·05 and 0·1 for pressure and other variables, and equal to 0·001 for all valuables in overall iterative sweeps.

4.0 DISCUSSION OF RESULTS

4.1 INVISCID CALCULATION

The flow around a Joukowsky aerofoil of 11% thickness, 2·4 % camber with a spoiler of height h = 10% located at the 70% chordwise position is considered in this investigation. The numbers of the elements are 58 on the aerofoil, five on the spoiler, 18 on the separation streamline from the spoiler tip, and 11 on the separation streamline from the trailing-edge.

The predicted surface pressure distribution on the aerofoil at an incidence $\alpha = 12°$ with the spoiler inclination $\delta = 90°$ is shown in Fig. 4 and compared with experimental results[2] where $\alpha = 13°$. It is shown that the overall prediction is in reasonable agreement with the experimental result except near the leading-edge and just upstream of the spoiler. This may be due to the inaccurate prediction of the circulation about the aerofoil and to the separation bubble just in front of the spoiler. Figure 5 compares the calculated C_L variation

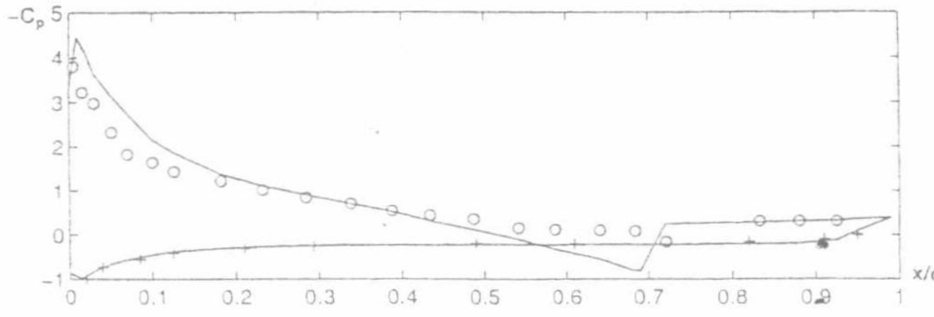

Figure 6. Pressure distribution on Joukowsky aerofoil,
$h = 0{\cdot}1c$, $e = 0{\cdot}7c$, $\alpha = 12°$, $\delta = 30°$
(— panel method; +o experimental[6])

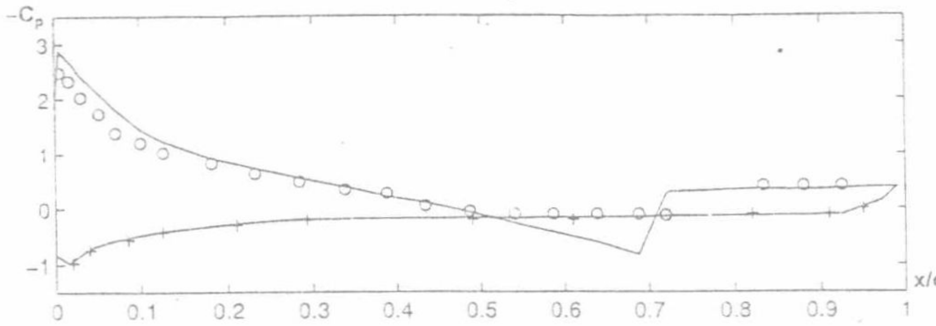

Figure 7. Pressure distributions on Joukowsky aerofoil
$h = 0{\cdot}1c$, $e = 0{\cdot}7c$, $\alpha = 12°$, $\delta = 60°$
(— panel method; +o experimental[6])

with respect to aerofoil incidence at $\delta = 90°$ from the inviscid calculation and experimental results[7]. It is necessary to point out that the good agreement in C_L may be due to some cancellation of lift from inaccurate predictions of pressure near the leading-edge and in the region upstream of the spoiler. Similarly, reasonable agreements are found between the predicted and measured results[3] of surface pressure distribution with aerofoil incidence $\alpha = 12°$ and spoiler inclination $\alpha = 30°$ and 60°, as depicted in Figs 6 and 7.

4.2 Viscous calculation

A 42 × 64 conventional H-mesh[13] is used in the flowfield around the same Joukowsky aerofoil because it is easier to use the H-mesh to include the spoiler to the aerofoil surface, as shown in Fig. 8, than other types of mesh. In earlier calculations, finer meshes were tried. The results show that finer meshes require longer computational time for the same convergence criterion. However, the pressure distribution on the aerofoil surface has not gained much improvement. The numerical study here is focused on the large structure of the flow and to obtain reasonable lift prediction. Because no detail flow measurement is available for comparison, the above mentioned mesh size was chosen to keep the computational time to a minimum. The computational CPU time is about 610 to 680 seconds on a Power Challenge workstation. However, the computational time of the panel method in the inviscid calculation is about 50 to 90 seconds on the same workstation.

One of the disadvantages of inviscid computation is that it does not offer any computation of the flowfield such as the one shown in Fig. 9, which is obtained by CFD with the aerofoil at $\alpha = 0°$. As seen, a re-circulating bubble is found behind the spoiler and bound by the shear layer from the aerofoil tip and the upper surface of the aerofoil near the trailing-edge. This bubble extends beyond the trailing-edge and has a length about 0·2 ~ 0·25 chord. This agrees with the assumption in the inviscid calculation that the shear layers from the spoiler tip and the aerofoil trailing-edge become thin vortex sheets and that these sheets enclose a bubble downstream of the spoiler. The wake length found is close to the result obtained from Equation (7). Although small in size, there is another re-circulating zone just upstream of the spoiler, as indicated in Fig. 9. This re-circulating zone is found in pressure measurements[2, 3, 7] but not dealt with in inviscid flow models.

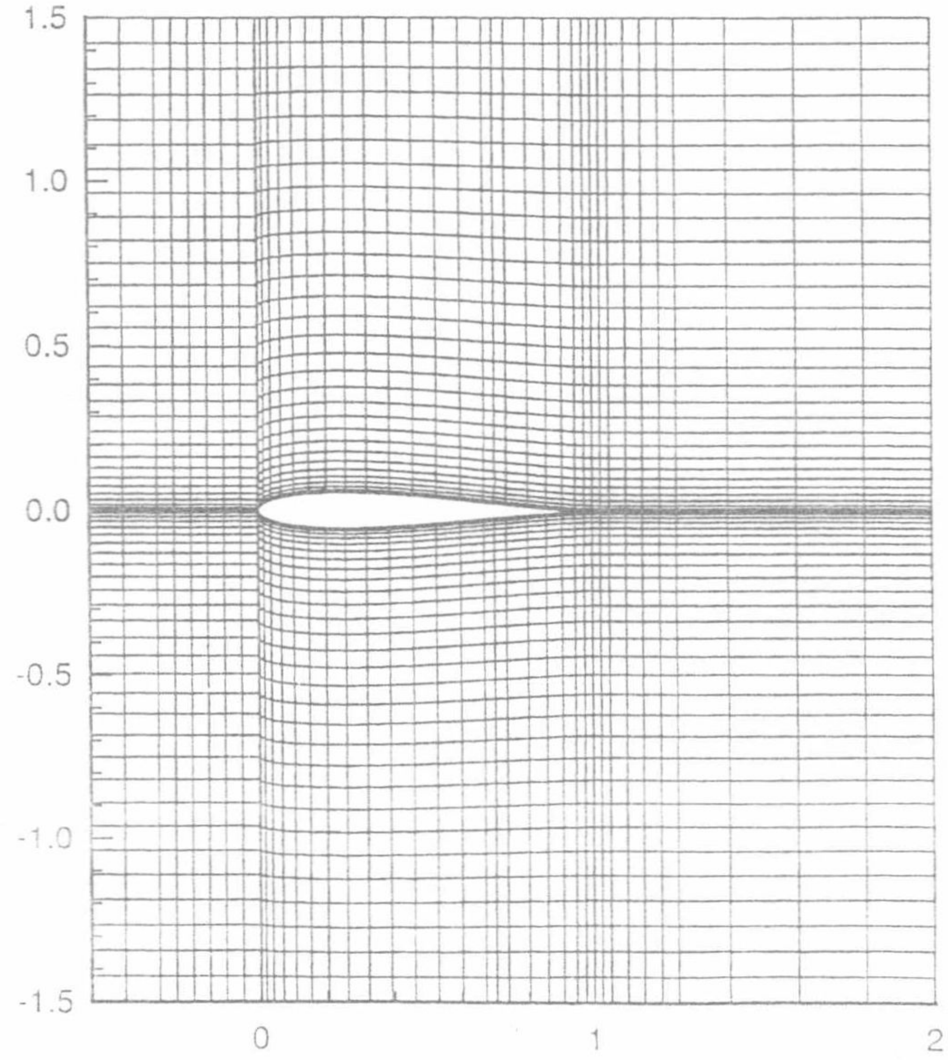

Figure 8. Overall grid structure.

The predicted pressure distribution on the aerofoil surface at $\alpha = 12°$ is also shown in Fig. 4 as compared with the inviscid method and experimental results. The Navier-Stokes computation is in better agreement with the experimental result. From Fig. 5, the predicted values of C_L from the two methods are in good agreement with the experimental results. The comparison of the two methods shows that the panel method is still a good engineering method which gives a reasonable lift for the aerofoil with the spoiler at smaller computational cost.

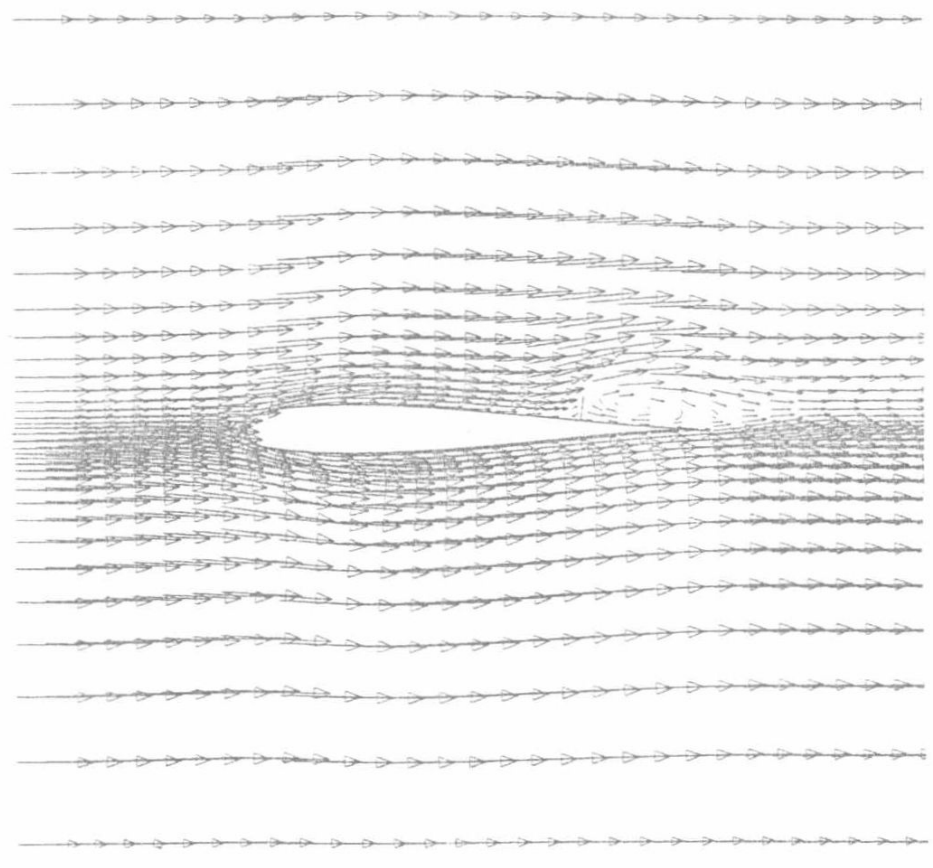

Figure 9. Computed flow field around Joukowsky aerofoil with spoiler.
($h = 0{\cdot}1c$, $e = 0{\cdot}7c$, $\alpha = 0°$, $\delta = 90°$)

5.0 CONCLUSION

An inviscid model and a Navier-Stokes code have been developed to numerically study the steady flow around an aerofoil with a spoiler. The results show that both inviscid and viscous methods can provide reasonable predictions of pressure and overall lift. However, the computational time of the panel method is significantly less than that required by the Navier-Stokes calculation. Detail prediction of spoiler performance still requires the use of the Navier-Stokes computation. Only the Navier-Stokes simulation can offer an overall prediction of the flow field, including separation both upstream and downstream of the spoiler.

In this study, it is found that when the Navier-Stokes computation is carried out, further research is still needed in finding a more suitable mesh generating method, which can be used for any spoiler inclination and turbulence models. Detail measurements on the vortical structure of the flow are needed to provide information to refine the computational results. The unsteady flow induced by a moving spoiler is an interesting and challenging problem because it requires a powerful code to generate the moving mesh.

REFERENCES

1. Woods, L.C. Theory of aerofoils on which occur bubbles of stationary air, ARC R&M 3049, 1953.
2. Pfeiffer, N.J. and Zumwalt, G.W. Computational model for low speed flows past aerofoils with spoilers, *AIAA J*, **20**, (3), pp 376-381.
3. Woods, L.C. Theory of aerofoil spoilers, ARC R&M 2969, 1953.
4. Barnes, C.S. A developed theory of spoiler on aerofoils, ARC CP 887, 1965.
5. Jandali, T. and Parkinson, G.V. A potential flow theory for airfoil spoilers, *Trans CASI*, March 1970, **1**, (3).
6. Parkinson, G.V. and Yeung, W.A. Wake source model for airfoils with separated flow, *J Fluid Mech*, 1987, **179**, pp 41-57.
7. Tou, H.B. and Hancock, G.J. Inviscid theory of two-dimensional aerofoil/spoiler configurations at low speed, Part I: Some experiences on simple panel methods applied to attached and separated flows, Part II: Steady aerofoil-spoiler characteristics, *Aeronaut J*, October 1987, **91**, (908), pp 350-366.
8. Maskew, B. and Dvorak, F.A. The prediction of C_{Lmax} using a separated flow model, *J Am Heli Soc*, 1978, **23**, pp 2-8.
9. Lewis, R.I. *Vortex Element Methods for Fluid Dynamic Analysis of Engineering Systems*, Cambridge University Press, 1991.
10. Parkinson, G.V. and Tam Doo, P. Prediction of aerodynamic effects of spoilers on wings, AGARD CP 204, 1976.
11. Elkaim, D., Reggio, M. and Camarero, R. Simulating two-dimensional turbulent flow by using the k-ε model and the vorticity-streamfunction formulation, *Int J Numer Methods in Fluids*, 1992, **14**, pp 961-980.
12. Amano, R.S. Development of a turbulence near-wall model and its application to separated and reattached flows, *Numerical Heat Transfer*, 1984, **7**, pp 59-75.
13. Thompson, J.F., Warsi, Z.U.A. and Mastin, C.W. *Numerical Grid Generation: Foundations and Applications*, North-Holland: Elsevier Science Publishing, 1985.
14. Patankar, S.V. *Numerical Heat Transfer and Fluid Flow*, Hemisphere/McGraw-Hill, New York, 1980.
15. Pun, W.M. and Spalding, D.B.A. General computer program for two dimensional elliptic flows, Imperial College, London, Mechanical Engineering Report HTS/76/2, 1976.
16. Xu, C. and Guo, R.W. An effective method for numerical simulations of separated flows, *Acta Aerodynamica Sinica*, 1994, **12**, pp 363-367.

振荡管内气柱谐振的研究

李学来　郭荣伟

（南京航空航天大学动力工程系，南京，210016）

ON RESONANCE OF GAS COLUMN IN AN OSCILLATORY TUBE

Li Xuelai, Guo Rongwei

(Deparment of Power Engineering, Nanjing University of Aeronautics & Astronautics, Nanjing, 210016)

摘　要　首次提出振荡管气柱谐振概念。对气柱谐振机理、条件、有关因素对谐振激励频率的影响及谐振状态下管内振荡流特性进行了探讨。结果表明：气柱谐振与管内激波运动有关；谐振状态下管内出现最强的压力波并产生最强的冷效应和热效应。

关键词　振荡流　谐振　激波　直接膨胀制冷

中图分类号　TQ051.5，TK124

Abstract　A new concept, gas column resonance, was established. The mechanism and condition of gas column resonance, the influences of some factors on resonant frequencies, and the resonant features were investigated. The results show that the resonance is connected with the movement of the shock wave. The pressure wave strength, the cooling effect and heating effect of the tube are the strongest in a state of resonance.

Key words　oscillatory flow, resonance, shock wave, direct expansion refrigeration

70 年代初，法国 NAT 公司研究发现，用高速脉动射流周期性地激励一端开口而另一端封闭的匀直管，使管内原有静止气体产生振荡，可产生强烈的热效应和冷效应[1]。基于这些效应而形成的气体膨胀制冷技术，具有设备结构简单、操作维护容易及制冷速率大等优点，因而在石油化工、能源工程、航空航天等领域中有广阔的应用前景。

振荡管虽然结构简单，但由于管内非定常流动伴随着非定常传热，同时还存在质量掺混、摩擦、开口端大量的粘性分离及波系间复杂的相互作用等真实效应，使得管内流动十分复杂，国外这方面的研究报道仅限于工业应用及专利方面，国内在振荡管结构、特性及应用方面做了大量的工作[2]，主要包括结构型式、射流激励频率(f_e)、管长(L)、膨胀比(ε)及管壁传热等因素对振荡管冷效应的影响。邵件[3]、方曜奇等[4]发现：在一定结构及工况下，振荡管存在一个最佳的射流激励频率(f_{opt})，当 f_e 偏离 f_{opt} 时，振荡管的制冷效率将显著下降，并发现 L 及 ε 是影响 f_{opt} 大小的两个主要因素。如何对振荡管的结构参数及工况参数进行匹配使其工作在 f_{opt} 状态下是振荡管设计的关键问题。目前的解决办法是通过大量实验拟合出 f_e、L、ε 之间的最佳匹配经验公式以指导设计。然而，进一步的研究表明，影响 f_{opt} 的因素远不止 L、ε 这两个因素，如管外换热状况也对 f_{opt} 存在重要影响[5]。因此，深入研究最佳射流激励现象的内在机制对解决振荡管参数间的最佳匹配问题及了解振荡管制冷机理有重要意义。本文提出振荡管气柱谐振概念，并对气柱谐振机理、条件及该状态下管内振荡流特性进行了探讨。

1　气柱谐振现象与机理

不同 f_e 下振荡管内动态压力测量结果表明（见图 1），在振荡管结构及气流参数一定的情况下，当 f_e 为某一固定值时，管内出现最强的压力波。而当 f_e 偏离（大于或小于）该值时，入射压力波强度都将减弱。本文将这一现象称为管内气柱谐振。并将此时管内气柱的振荡频率称为谐振频率，记为 f_{gr}；将此时的射流激励频率称为谐振激励频率，记为 f_{er}。

由于使管内气柱产生振荡的能量主要由入射激波提供，因此，气柱谐振现象与管内激波运动密切相关。为便于分析，作如下基本假定：管内为一元流动；管内流体为理想气体；充、排气切换瞬时完成。在此基础上得到管内简化流动波图如图 2 所示。

根据反射激波到达管开口端的时间的不同可能出现以下 3 种情况：①反射激波先于接触面到达开口端；②反射激波与接触面同时到达开口端；

1998-[illegible] 收到，1998-[illegible] 收到修改稿

国家自然科学基金([illegible])及中国博士后科学基金资助课题

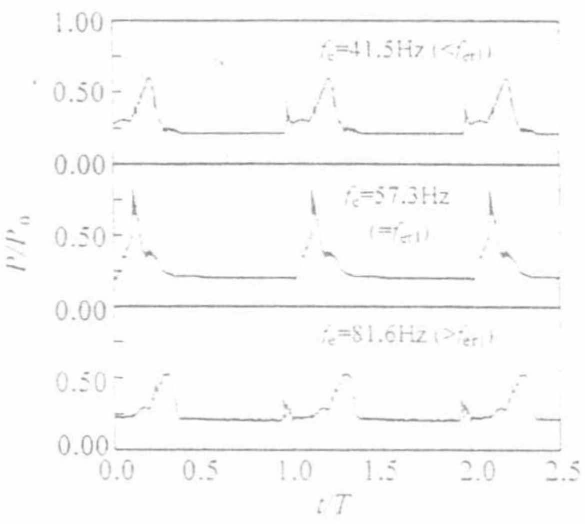

图 1　管内压力波形测量结果

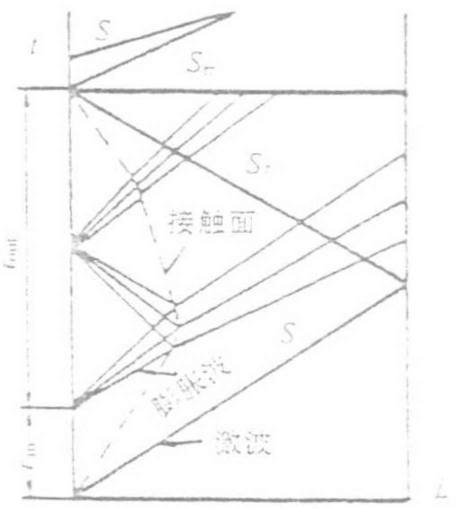

图 2　管内流动波图

③接触面先于反射激波到达开口端。图 2 描述的是情况②时的管内波的运动。先分析情况②：由于排气完毕时，喷管后沿经过开口端而将其封闭，在开口端形成一个固壁边界。本周期的反射激波 S_r 到达开口端时便再次反射为一道与入射激波 S 同方向运动的反射激波 S_{rr}。当下一个充排气周期的入射激波 S 赶上 S_{rr} 时，便叠加为一道比 S 更强的入射激波。再看情况②、③：在这 2 种情况下，当反射激波 S_r 到达开口端时，开口端仍与低压排气室相连通，则 S_r 在开口端必然反射为一束右行膨胀波。当下一个周期的入射激波 S 赶上该膨胀波束时，激波强度将被削弱。这就是产生气柱谐振的内在原因。

2　气柱谐振条件

上述气柱谐振机理分析表明，当反射激波与接触面同时到达开口端时，便产生气柱谐振。因此，激波传播经历 2 倍管长行程所需的时间刚好等于气柱振荡周期时间。即

$$2L/W = 1/f_{gr} \tag{1}$$

式中：L 为管长；W 为激波传播速度。另外，接触面返回到开口端意味着一个充、排气周期的结束，即气柱谐振周期时间等于充、排气周期时间。因此，气柱谐振频率应等于此时的射流激励频率，即

$$f_{gr} = f_{er} \tag{2}$$

将式(2)代入式(1)得

$$f_{er} = W/(2L) \tag{3}$$

其中：W 为激波传播速度。W 可由下式给出

$$W = Ma \cdot a_1 \tag{4}$$

式中：Ma 为激波马赫数；a_1 为波前气体音速，$a_1 = \sqrt{\gamma R T_1}$，其中：$\gamma$、$R$、$T_1$ 分别为气体的比热比、气体常数及波前气体温度。Ma 由下式给出[3]

$$\varepsilon = \{1 - 2(\gamma - 1)(Ma - 1/Ma)^2/[\alpha(\gamma - 1)^2]\}^{\gamma/(1-\gamma)} \cdot (2\gamma Ma^2 - \gamma + 1)/[(\gamma - 1)\beta] \tag{5}$$

式中：α 为进气滞止温度与①区气体温度之比；β 为排气背压与①区气体压力之比。

在前述基本假设下，当射流激励频率呈整数倍(如 k 倍)提高时，本周期的反射激波将在第 k 个周期与接触面同时到达振荡管的开口端，仍能产生气柱谐振。因此有

$$f_{erk} = kW/(2L) \tag{6}$$

其中：$k = 1, 2, 3, \cdots\cdots$。由式(6)可知，当结构参数及气流参数一定时，振荡管存在多阶谐振：$k=1$ 时，称为一阶谐振，此时的射流激励频率称为一阶谐振激励频率 f_{er1}；$k=2$ 时，称为二阶谐振，此时的射流激励频率称为二阶谐振激励频率 f_{er2}……依此类推。

由式(6)还可以看出，高阶谐振激励频率为一阶谐振激励频率的相应整数倍，即 $f_{erk} = kf_{er1}$。下面分析有关因素对谐振激励频率的影响：

(1) 膨胀比 ε 的影响　随着 ε 的增大，Ma 及 a_1 均增大，由式(4)知，W 将增大。再由式(6)知，谐振激励频率将升高。

(2) 管长 L 的影响　由式(6)知，f_{erk} 与 L 成反比，即 f_{erk} 随 L 的增大而降低，反之亦然。

(3) 管外换热状况的影响　管外换热状况越好，则管内气体的温度就越低，a_1 便越小。尽管由式(5)知此时 Ma 将略有增大，但由于 T_1 下降导致 a_1 降低的幅度要远大于 Ma 的增幅，从而使 W 减小，由式(6)知，f_{erk} 将降低。

以上分析了一些主要因素对 f_{erk} 的影响，所得结论与有关实验结果[2]相吻合。由式(6)还可分析其它因素对 f_{erk} 的影响。

3　气柱谐振特性

本文对谐振状态下管内振荡流特性进行了实验研究。实验中，振荡管采用内径为 12mm、壁厚

1mm、长 3.0m 的紫铜管,膨胀比 $\varepsilon=2\sim6$;管内流体介质为空气。管内动态压力用微型压电晶体传感器及数据采集系统测量;壁温分布用 8 付经标定的镍铬一考铜热偶及数据采集系统实现多点同步测量;射流激励频率则是通过测量气体分配器的转速 n,然后由下式计算得到

$$f_e = Nn/60 \tag{7}$$

式中:N 为气体分配器上射气孔的个数。

图 1 为一阶谐振激励频率 $f_{er1}=57.3$Hz 及其附近 2 个射流激励频率(41.5Hz 和 81.6Hz)下,管内压力波形的测量结果。由图 1 知,在气柱谐振状态下,管内形成的压力波最强,其波峰幅值比非谐振状态下高 30%以上。图 3 为振荡管制冷效率(η)随 f_e 变化的实验结果。由图 3 知,η 随 f_e 的变化而出现多个峰值,峰值点与低谷点的效率可相差 10%以上,各峰值所对应的 f_e 即为各阶谐振激励频率 f_{erk}。当 f_e 偏离 f_{erk} 时,由于反射激波穿过部分低温排气区,对这部分排气产生加热作用,从而使 η 降低。从图 3 还可以看出,各峰值所对应的 f_e 近似地成倍数关系,这与前述分析基本吻合。但是,越往后面的峰值,其对应的 f_e 值偏离第 1 个峰值所对应的 f_e 值的相应整数倍的程度越大($f_{erk}<kf_{er1}$),这主要是由于振荡管 L/D 值大,在粘性和摩擦作用下,激波尤其是多次反射激波在传播过程中衰减严重,从而使激波速度减小所导致的。图 4 为振荡管壁温分布测量结果。当管外换热状况一定时,振荡管热端壁温的高低反映了管内振荡流热效应的强弱。由图 4 知,谐振状态下的热效应最强。这主要是由于谐振状态下管内形成的入射激波最强,因而激波对管内气柱的加热作用最强所导致的。

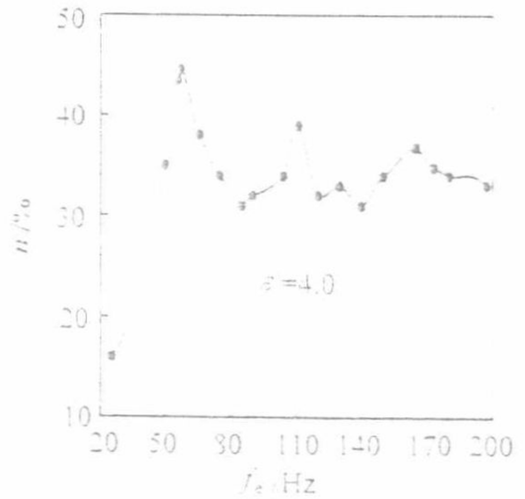

图 3　制冷效率随 f_e 的变化

以上实验结果表明,在气柱谐振状态下,振荡管可获得最佳性能。因此,式(6)不仅是产生气柱谐振的条件,同时,也是一个包含振荡管结构参

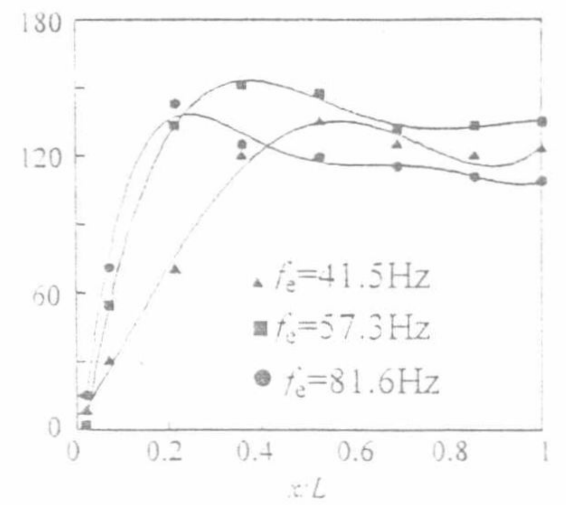

图 4　壁温分布

数、气流参数及运行参数的最佳匹配关系式。值得指出的是,本文讨论的是一维模型管内的纵向振荡,而实际中,由于喷管旋转扫过振荡管开口端,将使管内气柱产生横向振荡。因此,本文给出的有关关系式适用于小管径、大管长的振荡管(目前国内研制的振荡管管径为 $D=8\sim12$mm,长径比为 $L/D=150\sim350$),而对于大 D 或小 L 的振荡管将引起较大误差。

4　结　论

(1) 当射流激励频率等于管内气柱振荡频率的整数倍时便产生气柱谐振,凡是影响激波运动(包括激波传播速度及运动行程)的因素都将影响谐振激励频率值的大小;

(2) 气柱谐振状态下振荡管内出现最强的压力波,同时产生最强的冷效应和热效应;

(3) 本文提出的振荡管结构参数、气流参数及运行参数的最佳匹配关系(即气柱谐振条件),可为波制冷机的优化设计提供理论指导。

参　考　文　献

1　Rennaz M C. Wellhead gas refrigerator field strips condensate. World Oil, 1971, 60～61

2　李学来. 压力波制冷机的研究与工业开发. 制冷, 1997 (3): 6～12

3　邓伴, 沈永年. 转动式热分离器转速与管长匹配研究. 浙江大学学报, 1988, 22(5): 114～119

4　Fang Y Q, Zheng J. Experimental study of gas wave refrigeration. Shock Wave Proc. Sendai, Japan, 1991, 2: 1335～1338

5　俞鸿儒. 热分离器内的流动. 大连工学院学报, 1984, 23(4): 1～7

李学来　男,1966 年 8 月生,南京航空航天大学航空与宇航技术在读博士生,已发表"振荡管中的热流体流动"等论文 20 余篇。

第 20 卷 第 3 期
1999 年 5 月

航空学报
ACTA AERONAUTICA ET ASTRONAUTICA SINICA

Vol. 20 No. 3
May 1999

文章编号:1000-6893(1999)03-0205-06

直管斜切式方转圆进气道的电磁散射特性及抑制技术的实验研究

廖 伟, 郭荣伟
(南京航空航天大学 动力工程系, 江苏 南京 210016)

EXPERIMENTAL RESEARCH OF RCS AND RCSR OF A STRAIGHT RECTANGLE-TO-ROUND SCOOP INLET

LIAO Wei, GUO Rong-wei
(2nd Dept., Nanjing University of Aeronautics and Astronautics, Nanjing 210016, China)

摘 要:从进气道的雷达散射截面着手,通过实验研究了直管斜切式方转圆进气道在各种状态下的电磁散射特性,分析了终端、攻角对其电磁散射特性的影响,并进一步提出了该型进气道的雷达截面减缩措施,研究了吸波材料贴敷长度、贴敷位置以及消波器等对雷达截面减缩效果的影响。为有效改善该型进气道的电磁散射特性提供了技术依据。

关键词:进气道;电磁散射;雷达截面;雷达截面减缩

中图分类号:V228.7　　　文献标识码:A

Abstract: The Radar Cross Section (RCS) of a straight rectangle-to-round scoop inlet has been investigated. It includes the influences of the attack angle and termination on the electromagnetic scattering characteristics. Then the measurements of the Radar Cross Section Reduction (RCSR) of the inlet are put forward. At the same time, the effects of length, position of absorbing-wave material and absorbing-wave grille on RCSR are further studied. As the results indicate, the measurements suggested here have put very distinct effect on decreasing RCS of the inlet. This paper affords a technological basis for efficiently improving the low-observable inlets.

Key words: air inlets; electromagnetic scattering; RCS; RCSR

飞行器进气道是雷达波的强散射源之一[1],为了较大幅度地降低飞行器的雷达散射截面(Radar Cross Section,简称 RCS),必须对进气道采取特殊的技术措施。直管斜切式方转圆进气道气动性能优良,但其雷达散射截面过大,是增大整机雷达散射截面的重要因素之一,必须尽可能地减小该进气道的雷达散射截面。由于目标本身形状结构的复杂性以及电磁场边界条件的限制,对电磁散射领域中目标的 RCS 值的精确理论分析十分困难,实验成为一个主要的研究手段[2]。

基于以上认识,本文的实验研究将包括以下两个方面的工作:①分别研究在不同终端、不同攻角等条件下,该进气道的电磁散射特性;② 进一步研究其雷达散射截面减缩措施(RCSR 技术),包括加消波器及在进气道内壁面贴敷吸波材料等,以期寻找到合理的吸波材料贴敷长度及位置,并考察消波器的 RCSR 效果,为减缩该型进气道的 RCS 提供切实可行的方案。

1 实验模型及测试设备

实验用的进气道模型如图 1 所示。该模型为木质,具有单斜切式唇口,从上唇口处起至终端出口全长 1095mm,其中唇口段长 245mm,内管道长 850mm,内管道由 300mm 的方柱段、283mm 的方圆过渡段及 267mm 的圆柱段组成,其中最末段为一长度等于出口截面直径的等截面圆柱段。该模型进口截面大小为 135mm×120mm,出口截面内径 D 为 170mm,模型管道内壁贴敷有铝箔材料,铝箔平整光滑,使电磁散射实验不受表面质量的影响,该进气道的下壁面上装有外物防护孔板,在模型上为一块按比例缩小的金属板,其上

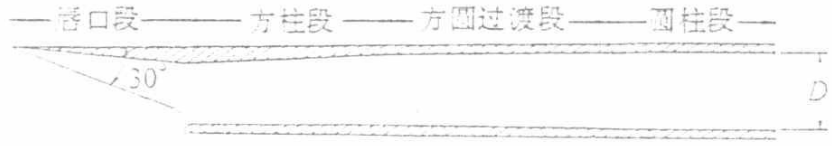

图 1 直管斜切式方转圆进气道模型图

收稿日期:1998-06-08;修订日期:1998-08-01

也有交错排列的小孔，直径为 3mm，孔的中心距为 6mm，整块金属板的尺寸为 250mm×120mm。

实验工作是在南京航空航天大学无人机研究所的微波暗室进行的。暗室尺寸为 28m×8.5m×8.5m，实验时背景电平为 −43dBsm。实验时模型与天线之间的距离为 11.5m。该暗室目前有 3 个波段（X、K_u、K_a）的发射和接收装置系统。本实验在 X 波段下进行，其频率为 $f = 9375\text{MHz}$。由于该暗室安装了激光瞄准器和光栅编码器，使实验模型的位置、安放姿态和方位角均得到准确地控制，提高了测定结果的可靠性。

为了保证目标 RCS 的测量精度，必须使进气道模型与天线之间的距离满足远场条件，即 $R \geqslant 2a^2/\lambda$[1]。在本文中 $R = 11.5\text{m}$，$\lambda = 32\text{mm}$，$a = 120\text{mm}$，显然满足远场条件。为了消除地面的影响，微波暗室地面铺有吸波材料，而且使目标架设高度 $H = 3.4\text{m}$。由于本文主要关心进气道内部及口径边缘的散射场，因此在进气道模型外部贴有吸波材料，以消除其外表面的影响。

2　进气道的电磁散射特性研究

本实验测量了该型进气道模型在不同攻角、不同终端等状态下的雷达散射截面。这里的不同终端是指进气道终端分别为短路、静止转子和转动转子；不同攻角是指攻角大小分别为 0°、5°、10°。

2.1　不同终端对进气道散射特性的影响

为便于分析，这里仅以 0°攻角时为例，分别对 3 种终端状态的影响进行两两比较。

如图 2 可以看出，在几乎所有的方位角范围内，如果其它状态完全相同，终端短路时的 RCS 值明显高于终端为静止转子和终端为转动转子时的 RCS 值，其差值高达近 10dB 甚至 10dB 以上；

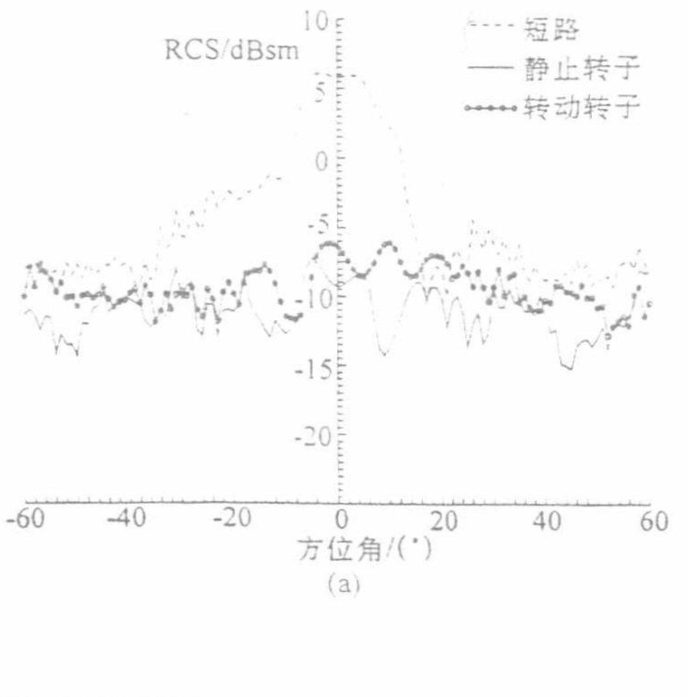

(a)

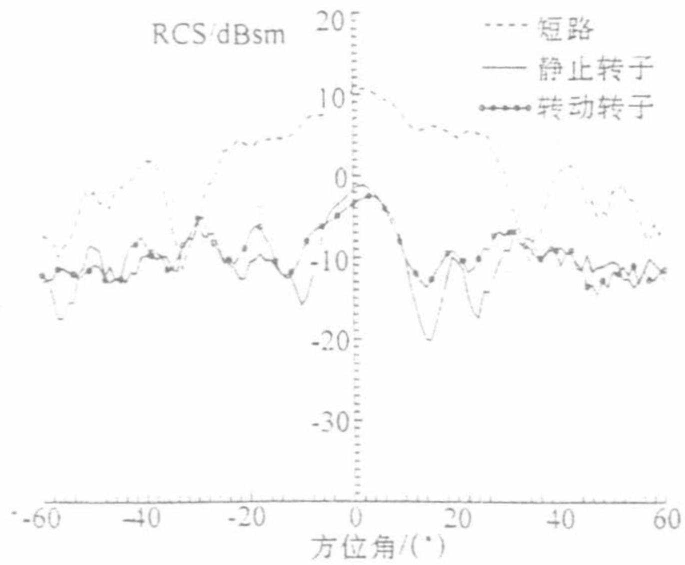

(b)

图 2　0°攻角下，3 种不同终端的 RCS 值比较曲线

(a)水平极化；(b)垂直极化

终端为静止转子时的 RCS 值和终端为转动转子时的 RCS 值相差不大。后者比前者略高，差值一般在 1～3dB 之间。当攻角为 5°和 10°时，可以得到大致相同的结论。

2.2　不同攻角对进气道散射特性的影响

图 3 给出了终端为短路时不同攻角下的

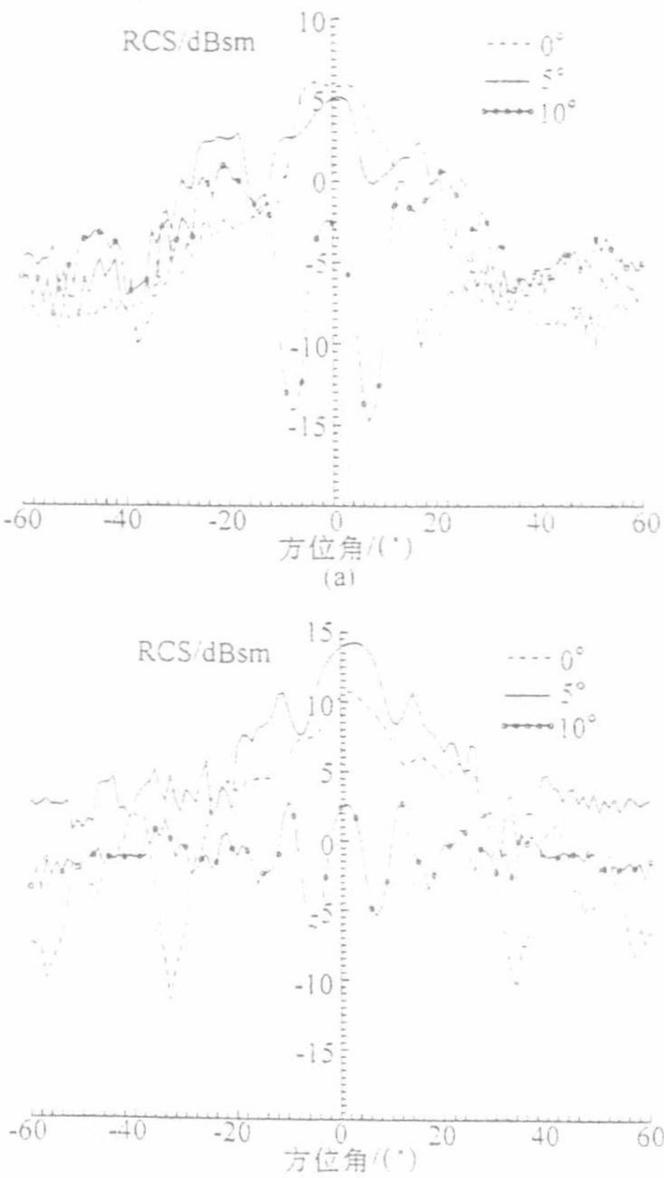

(b)

图 3　终端为短路时，不同攻角下 RCS 值比较曲线

(a)水平极化；(b)垂直极化

RCS 值比较曲线。如图 3 所示，水平极化时，在大约 ±15°方位角范围内，0°和 5°攻角的 RCS 曲线

明显高于 10°攻角的 RCS 曲线；在 0°方位角附近，0°攻角的 RCS 曲线比 5°攻角的 RCS 曲线略高，但就较大方位角范围而言，则前者比后者低。垂直极化时，0°和 5°攻角时的 RCS 曲线也明显高于 10°攻角时的 RCS 曲线，而 0°攻角时的 RCS 曲线却比 5°攻角时的 RCS 曲线略低。当终端分别为静止转子和转动转子时，可得出同短路时基本一致的结论，因此在 0°、5°、10° 三种不同大小的攻角中，如果其它状态完全相同，一般说来，10°攻角时的 RCS 值最小、5°攻角时的 RCS 值最大。

3　进气道的雷达截面减缩研究

该实验将研究该型进气道雷达散射截面的减缩措施及其效果。适用于本文实验的 RCS 减缩措施只有雷达吸收技术，包括在进气道内壁贴敷吸波材料和在进气道后部加消波器。本节研究了吸波材料的 4 种贴敷长度。这里所说的 4 种长度均是指吸波材料的长度相当于进气道内通道长度的比例，分别为 1/2 长度、1/3 长度、1/4 长度和 1/5 长度。除 1/2 长度外，其余每一种贴敷长度的吸波材料均有 3 种贴敷方式，这 3 种方式是由唇口贴、前贴和后贴组合而得。

贴敷方式如图 4 所示，所谓唇口贴是指唇口（a 段）贴敷有吸波材料，前贴是指进气道模型内通道前部（b 段）贴敷有吸波材料，后贴是内通道后部紧靠消波器位置处（c 段）贴敷有吸波材料，全贴就是指 a、b、c 3 段均贴有吸波材料，全金属则是指 a、b、c 段均不贴吸波材料，即整个进气道内壁都是金属的。至于唇口贴一前贴则是指 a、b 段贴有吸波材料，而 c 段不贴，其余贴敷方式表示的意义可由此类推。若吸波材料贴敷过多，将造成进气道的重量及成本大大增加，就 1/2 长度而言，全贴意味着整个进气道内壁贴满吸波材料，因此，在该长度下将不考虑全贴和前贴＋后贴。对于每一种贴敷方式，均分为加消波器和不加消波器两种状态。

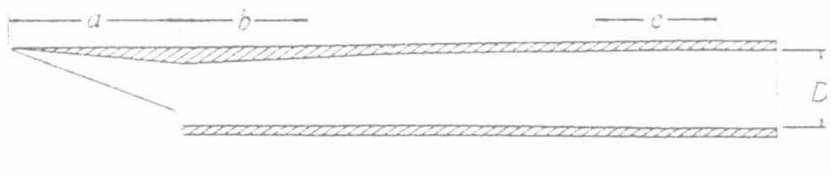

图 4　进气道模型吸波材料贴敷位置示意图

表 1 给出了方位角范围内 4 种长度的吸波材料在各种状态下相对于全金属的 RCS 平均值的下降 dB 数。很显然，表 1 中的值越大说明其减缩效果越好。

表 1　在方位角±15°内，各种状态相对于全金属的 RCS 平均值下降 dB 数

极化方式		水平极化				垂直极化			
贴敷方式	有无吸波器	1/2 长度	1/3 长度	1/4 长度	1/5 长度	1/2 长度	1/3 长度	1/4 长度	1/5 长度
全贴	有		10.68	7.96	7.91		12.13	13.01	7.71
	无		13.36	7.06	6.69		5.52	6.36	4.43
唇口贴	有	8.32	3.98	11.52	3.57	5.95	5.56	3.41	5.69
后贴	无	5.31	7.43	6.46	5.25	0.39	6.36	5.33	7.39
唇口贴	有	3.56	8.11	10.49	4.43	5.57	9.4	11.4	7.91
前贴	无	7.81	5.48	5.69	2.56	2.47	4.57	4.14	2.25
唇口贴	有	6.91	5.29	7.76	6.4	4.25	4.58	6.37	5.08
	无	0.37	1.32	1.68	1.34	2.6	3.45	3.99	4.72
全金属	有	6.29				3.30			
	无	0				0			
前贴	有	6.56	3.94	10.96	5.22	3.05	4.96	3.67	5.21
	无	4.59	2.61	4.12	2.07	3.42	3.82	3.65	0.86
前贴	有		3.37	7.78	6.36		3.1	3.78	5.19
后贴	无		5.76	5.78	3.99		3.61	3.31	6.38
后贴	有	6.98	6.34	8.37	5.6	5.82	7.42	7.13	5.35
	无	5.04	4.54	4.95	3.7	2.89	2.31	2.77	3.95

3.1　吸波材料长度对 RCS 减缩效果的影响

对于某一特定长度的吸波材料，不可能使目标在所有状态下的 RCS 平均值都达到最小，但如果使其在大多数情况下的 RCS 平均值最小，即其相对于全金属的 RCS 平均值下降 dB 数最大，则可以认为当吸波材料为这一长度时，其雷达截面减缩效果最好。在对表 1 进行初步观察之后，可以大致判断出 1/3、1/4 长度吸波材料的减缩效果要好一些。为便于比较，可以选定 1/4 长度的吸波材料（以下简称为 1/4 长度，其余类推）作为一个比较基准。这里先将 1/5 长度同 1/4 长度的情况